Fractal superconducting nanowire single-photon detectors working in dual bands and their applications in free-space and underwater hybrid LIDAR

Kai Zou,[1,2] **Zifan Hao,**[1,2] **Yifan Feng,**[1,2] **Yun Meng,**[1,2] **Nan Hu,**[1,2] **Stephan Steinhauer,**[3] **Samuel Gyger,**[3] **Val Zwiller,**[3] **and Xiaolong Hu**[1,2,*]

[1]*School of Precision Instrument and Optoelectronic Engineering, Tianjin University, Tianjin 300072, China*
[2]*Key Laboratory of Optoelectronic Information Science and Technology, Ministry of Education, Tianjin 300072, China*
[3]*Department of Applied Physics, Royal Institute of Technology (KTH), SE-106 91 Stockholm, Sweden*
*Corresponding author: xiaolonghu@tju.edu.cn

We demonstrate a fiber-coupled fractal superconducting nanowire single-photon detector (SNSPD) system with minimum polarization dependence of detection efficiency. Its system detection efficiency (SDE) was maximized at the wavelength of 1540 nm, which was measured to be $91 \pm 4\%$; furthermore, we observed the second local maximum of SDE at the wavelength of 520 nm, which was measured to be $61 \pm 2\%$. This dual-band feature of SDE was due to the enhancement of the optical absorptance by two longitudinal resonance modes of the micro-cavity. By using high SDE with minimum polarization dependence in these two bands, we implemented a hybrid LIDAR for imaging the remote objects in free space and under water. © 2023 Optica Publishing Group

In recent years, superconducting nanowire/microwire single-photon detectors with low polarization dependence of detection efficiency have attracted tremendous research interest. In Section 1 of Supplement 1, we list all the devices and their performances that have been reported in the literature. In particular, we demonstrated a fractal superconducting nanowire single-photon detector (SNSPD) system working at the telecommunication wavelength of 1575 nm with 84% system detection efficiency (SDE), 1.02 residual polarization sensitivity (PS), and 20.8-ps timing jitter [1]. The feature of high SDE for photons in all states of polarization (SoPs) is important, particularly for applications where the to-be-detected photons are in random SoPs and the SoPs are difficult to be controlled or adjusted [2–4]. Although researchers have previously reported multi-spectral meandering SNSPDs in several publications [5,6], polarization-insensitive SNSPDs that can work in more than one band remain unexplored. We present in this Letter a fiber-coupled fractal SNSPD system with minimum polarization dependence of SDE, working in dual bands. One is centered at the telecommunication

wavelength of 1540 nm, which falls in the technologically important bands for optical-fiber-based communication [7], free-space communication [8], and LIDAR applications [9]. The other is centered at the wavelength of 520 nm, the green-light band, which is technologically important for underwater light communications [10] and imaging [11]. We demonstrated an SDE of $91 \pm 4\%$ and $61 \pm 2\%$ at the wavelengths of 1540 nm and 520 nm, respectively, and a low PS of 1.01 at both wavelengths. We used this system to implement a free-space and underwater hybrid LIDAR for imaging remote objects either in air or in water. The significance of this dual-band fractal SNSPD lies in that it can simultaneously work at two technologically important and interesting bands, expanding the application spaces of SNSPDs.

The design and the structure of the fractal SNSPD are similar to what we presented in Ref. [1], but with two important improvements. First, we optimized the fill factor of the fractal SNSPD to be 0.26, which further enhanced the optical absorptance of the device, compared with the fill factor of 0.31 used in Ref. [1], according to our optical simulation. Second, we expanded the photosensitive region of the fractal SNSPD from 10.2 μm×10.2 μm [1] to 12.16 μm×12.16 μm. As the SMF-28e optical fiber connected with high-index fiber (HIF) with reduced mode size through a mode-size adapter [1] had low transmittance for the green light at 520 nm, we removed the HIF and the mode-size adapter in the system and coupled the SNSPD directly with the SMF-28e optical fiber. The mode-field diameter of the SMF-28e optical fiber is 10.4 μm, larger than that of the HIF, 6.3 μm, at 1540-nm wavelength. The expansion of the photosensitive region is therefore necessary for ensuring high coupling efficiency. See Section 2 of Supplement 1 for the calculation of the coupling efficiency. We note that according to our simulation, the SMF-28e optical fiber supports 20 guiding modes at the wavelength of 520 nm. The mode-field diameter of the LP_{01} mode of the SMF-28e optical fiber at 520 nm was simulated to be 7.4 μm. For the electrical configuration of the nanowires, we still used the structure of 16 cascaded two superconducting nanowire
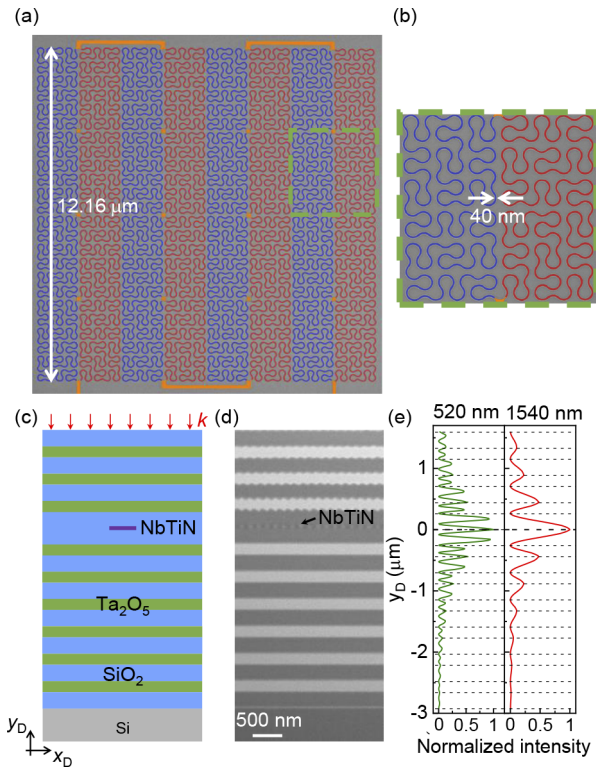
Fig. 1. Design and structure of a fractal SNSPD. (a) False-colored scanning electron micrograph of the fractal SNSPD, in which the photosensitive nanowires are colored in red and blue, and the auxiliary structures are colored in orange. (b) Zoom-in micrograph of the region enclosed in the green dashed box in panel (a). The width of the nanowire is measured to be 40 nm by scanning electron microscopy. (c) Schematics of its optical structure. From bottom to top are the silicon substrate, the bottom distributed Bragg reflector (DBR) composed of six pairs of Ta_2O_5 and SiO_2, the SiO_2 defect layer, and the top DBR composed of three pairs of Ta_2O_5 and SiO_2. The NbTiN nanowire is placed in the middle of the defect layer. Incident light illuminates the fractal SNSPD from the top of the structure. (d) Cross sectional scanning electron micrograph of the device. The cross sections of the NbTiN nanowires can barely be seen. (e) Light intensity distributions along y_D without nanowire at the wavelengths of 520 nm and 1540 nm, showing the first and second resonances of the optical microcavity.

Fig. 2. Detection efficiency of the fractal SNSPD. (a) Schematics of the experimental setup for measuring the system detection efficiency (SDE) in the green-light band. BS, beam splitter; NDF, neutral density filter; C, collimator; PC, polarization controller; OPM, optical power meter; TAC, time-to-amplitude converter. (b) Schematics of the experimental setup for measuring the SDE in the telecommunication band. A1, A2, A3, optical attenuators. (c) Simulated spectrum of optical absorptance, A, of the nanowire, and measured polarization-maximum SDE at various wavelengths. (d) Measured polarization-maximum and -minimum SDE at the wavelength of 520 nm, as a function of the bias current, I_b. (e) Measured polarization-maximum and -minimum SDE at the wavelength of 1540 nm, as a function of I_b. In these measurements, the fractal SNSPD was coupled with a piece of SMF-28e optical fiber.

avalanche photodetectors (2-SNAPs) [1]. Figure 1 presents the design of the fractal SNSPD and the structure of the resulting device. Figures 1(a) and 1(b) present the false-colored scanning electron micrographs of the fractal SNSPD. The superconducting film was 9-nm-thick NbTiN and the width of the nanowire was 40 nm, both remaining unchanged [1].

Figures 1(c) and 1(d) present the designed dielectric optical stacks composed of SiO_2 and Ta_2O_5 for enhancing optical absorptance and the cross sectional scanning electron micrograph. The thicknesses of each SiO_2 layer in the DBR, each Ta_2O_5 layer in the DBR, and the defect layer were 264 nm, 180 nm, and 529 nm, respectively. The NbTiN nanowires can also be seen, but very faintly, in the micrograph. Although the design of the optical structure was targeted at optimizing the optical absorptance in the infrared telecommunication wavelength near 1550 nm [1] using its lowest order resonance, we found a second-order resonance at the wavelength of 520 nm, which can also
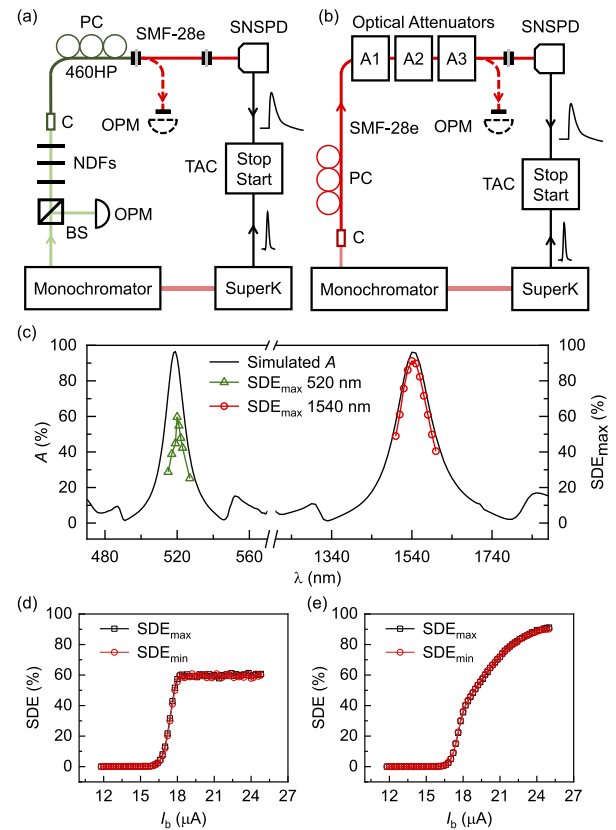
be used for enhancing the optical absorptance. We simulated the intensity distribution of these two modes using the software, COMSOL Multiphysics, and the refractive indices of the materials used are presented in Section 3 of Supplement 1. The simulated intensity distributions of these two modes, along the y_D direction, are presented in Fig. 1(e). We assumed that the nanowire is absent when we conducted the simulations.

We measured the SDE of the fiber-coupled SNSPD system using time-correlated single-photon counting (TCSPC) to effectively exclude the false counts [1,12]. SDE is defined as the total SDE including the transmittance of the optical fiber fed into the cryocooler. As we have already illustrated previously, the fractal SNSPD configured into the cascaded 2-SNAPs exhibited a false-count rate (FCR) higher than the dark-count rate (DCR) [1], but the FCR got close to the DCR at high bias currents. See Section 4 of Supplement 1 for the measurements and discussions regarding the DCR and FCR. To measure the spectrum

of the SDE, we used the experimental setups schematically presented in Figs. 2(a) and 2(b). We employed a supercontinuum light source (SuperK), filtered by a monochromator. The full widths at half maxima (FWHMs) of the spectra were both 2 nm. In Fig. 2(a), light was attenuated by three neutral density filters (NDFs) with their attenuation calibrated. The SoPs of light were adjusted by an in-line polarization controller, made of a 460HP optical fiber, which was connected to the SMF-28e optical fiber through a flange. The optical power in the SMF-28e was measured before inserting the three NDFs so that we calculated the optical power fed into the SNSPD system. Because the emission in the green-light band from the SuperK was relatively weak and the optical power after the monochromator was slowly drifting during the measurement, we used a beam splitter (BS) and another optical power meter to *in situ* monitor any changes of the optical power. Figure 2(b) presents the schematics of the experimental setup for measuring the SDE in the infrared telecommunication band, which is similar to that in Fig. 2(a), but simpler. The fractal SNSPD was packaged into a 0.1-W Gifford–McMahon cryocooler and the base temperature was 2.0 K. At this temperature, the switching current was measured to be 25.0 μA. The trigger signal from the SuperK was used as the start signal for TCSPC; and the output signal from the fractal SNSPD, after amplification by a low-noise cryogenic RF amplifier, was used as the stop signal.

Figure 2(c) presents the measured SDE_{max} in two bands as well as the simulated optical absorptance. To measure SDE_{max} in the telecommunication band, the fractal SNSPD was biased at 24.8 μA. The SDE_{max} and optical absorptance, A, both peaked at the wavelength of 1540 nm. The SDE_{max} was measured to be $91 \pm 4\%$, taking into account the fiber end-facet reflection occurring at the optical power meter [1] which would otherwise give a higher but false value of the SDE of 94%. Section 5 of Supplement 1 presents the calculation of the uncertainties of the SDE. The measured 91% SDE is, to date, the highest value ever measured on fractal SNSPDs. Here, A was simulated to be 96%. We note that for this particular device, the maximum A and SDE appear at the same wavelength, 1540 nm; however, they are more likely to occur at slightly different wavelengths, as we observed in our study and reported previously [1]. When we measured the SDE_{max} in the green-light band, the saturated plateau permitted us to bias the fractal SNSPD at, for example, 24.0 μA, which was 1.0 μA lower than the switching current. The SDE_{max} peaked at the wavelength of 520 nm, and A peaked at 519 nm. The SDE_{max} was measured to be $61 \pm 2\%$, also taking into account the correction due to the reflection at the optical power meter. The A was simulated to be 97% at the wavelength of 519 nm. We also measured the SDE of the fractal SNSPD coupled with a 460HP optical fiber, which is a single-mode fiber at the wavelength of 520 nm. The SDE_{max} and SDE_{min} were measured at this wavelength to be $72 \pm 3\%$ and $70 \pm 3\%$, respectively. The discrepancy between the expected and measured SDE might be due to the SDE in the green-light band being more sensitive to the fabrication-induced error in the device structure.

Figures 2(d) and 2(e) present the measured SDE as functions of bias current, I_b, at the wavelengths of 520 nm and 1540 nm, respectively. The SDE_{max} and SDE_{min} almost completely overlap each other, and the measured PS at the high bias current remains as low as 1.01. Another important feature is that the SDE measured at 520 nm shows a saturated plateau when the bias current exceeds 18.2 μA. Although this saturation at
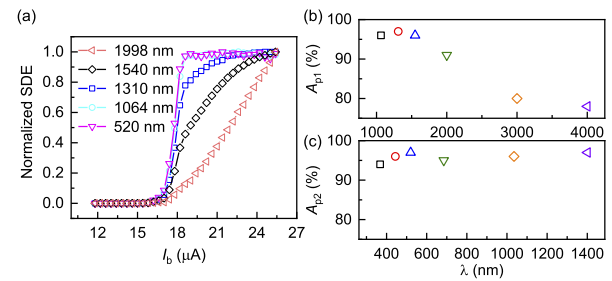

Fig. 3. Dual-band fractal SNSPDs designed for working at other wavelengths. (a) Measured normalized SDE, as a function of I_b, at the wavelengths of 520 nm, 1064 nm, 1310 nm, 1540 nm, and 1998 nm. (b) Simulated first peak optical absorptance, A_{p1}, enhanced by the first resonance of the optical microcavity. (c) Simulated the second peak optical absorptance, A_{p2}, enhanced by the second resonance of the optical microcavity.

a shorter wavelength than infrared telecommunication wavelengths is not surprising, it is the first time that the SDE of a fractal SNSPD was measured in the visible range, confirming the similar saturating trend of internal detection efficiency as most non-latching, meandering SNSPDs exhibit.

We discuss how to design and construct fractal SNSPDs with high SDE working in other dual bands as well as the potential challenges. For internal detection efficiency, we measured the normalized SDE as a function of I_b at several wavelengths, 520 nm, 1064 nm, 1310 nm, 1540 nm, and 1998 nm. Figure 3(a) presents the results. We note that for these measurements, we did not adjust the SoP of incident light and simply assumed PS to be 1. At 1064 nm, the curve shows a broad plateau, similar to that at 520 nm. At 1310 nm, a plateau still exists but with a decreased bias range for the plateau. At 1540 nm, the curve still shows a trend of saturation but without an apparent plateau. At 1998 nm, no saturation trend is observed, indicating the internal detection efficiency is less than 1 at 1998 nm or even longer wavelengths. The same concept of the enhancement of the optical absorptance in dual bands using the microcavity can be applied by re-designing the optical stacks. Figures 3(b) and 3(c) present the maximized peak optical absorptance, A_{p1} and A_{p2}, of the NbTiN nanowire in several groups of dual bands, 1064 nm and 368 nm, 1310 nm and 444 nm, 1550 nm and 520 nm, 2000 nm and 685 nm, 3000 nm and 1035 nm, and 4000 nm and 1401 nm. The refractive indices of the relevant materials are presented in Section 3 of Supplement 1. At the wavelengths of 2000 nm, 3000 nm, and 4000 nm, the material absorption of SiO_2 and Ta_2O_5 increases, affecting optical absorptance of the NbTiN nanowire. The decrease of internal detection efficiency and optical absorptance is among the challenges for making mid-infrared fractal SNSPDs with high SDE.

Using this dual-band fractal SNSPD, we implemented a time-of-flight, hybrid LIDAR that can image the remote objects in the free space or under water. The green-light band is commonly used for underwater detection because of the low optical absorptance; the infrared telecommunication band is used for free-space LIDAR because of being eye-safe and with low background of solar radiation. Figure 4(a) presents the schematics of the experimental setup. Broadband light emitting from the SuperK, filtered by the monochromator, was used as the light source. The wavelength, either 1540 nm or 520 nm, was selected by controlling the monochromator. The measured spectra, after
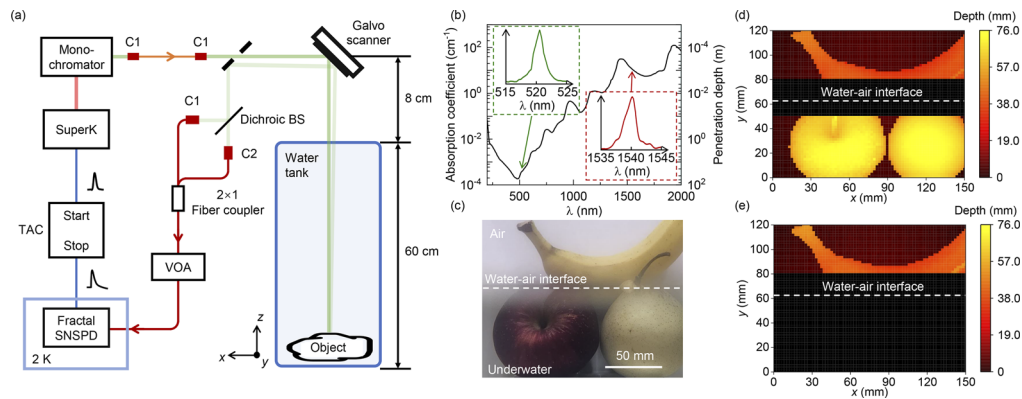
Fig. 4. Free-space and underwater hybrid lidar based on a fractal SNSPD. (a) Schematics of the experimental setup. C1 and C2, collimators; TAC, time-to-amplitude converter; VOA, variable optical attenuator; BS, beam splitter. (b) Spectrum of absorption coefficient and penetration depth of water. The data are from Ref. [13]. The insets are the spectra of output light from the monochromator, centered at 520 nm and 1540 nm. (c) Photograph of the objects, including an apple, a pear, and a banana, partly immersed in water in a tank. (d) False-colored image obtained by the LIDAR working at 520 nm with the contrast of depth. (e) False-colored image obtained by the LIDAR working at 1540 nm with the contrast of depth. The underwater part of the objects is invisible because of the large attenuation of light at 1540 nm by water.

being filtered, are presented in the insets of Fig. 4(b). In Fig. 4(a), the echo photons were coupled into an optical fiber either through collimator C1 or through collimator C2, according to the specific wavelength used in the LIDAR system. The absorption coefficient of water and the corresponding penetration depth presented in Fig. 4(b) are from Ref. [13]. In the green-light band, the absorption coefficient is approximately four orders of magnitude smaller than that at 1540 nm in the telecommunication band. The objects used here included an apple, a pear, and a banana, partly immersed under water, and partly above the water and in air. The material of the tank is acrylic. Figure 4(c) presents a photograph of the scene. In the photograph, a blurry layer exists at the water–air interface because the surface tension of water makes the interface a concave surface at the inner wall of the tank. When the camera focused on the objects at the rear, the concave surface at the front was out of focus. Figure 4(d) presents the LIDAR image with the contrast of depth, obtained by raster-scanning the objects using green light. The image reproduced the shape of the objects except for the blurry region near the water–air interface. At the interface, the beam was reflected by the interface toward another unwanted direction. In comparison, as presented in Fig. 4(e), raster-scanning using light at 1540 nm only yielded the image in the air and above the blurry region because the large attenuation of water at this wavelength prohibited imaging. In addition to the depth, the relative intensity was also used as another type of effective contrast, capable of reproducing the shape of the objects (Section 6 of Supplement 1). Therefore, such a hybrid LIDAR system can be shipborne for imaging objects in the air or under water.

In conclusion, we have demonstrated a fiber-coupled fractal SNSPD system working in dual bands with low polarization dependence of the SDE. In the telecommunication band, the maximum SDE was $91 \pm 4\%$ at 1540 nm; in the green-light band, the maximum SDE was $61 \pm 2\%$ at 520 nm. Furthermore, it is possible to engineer the device structure to target other dual bands for high SDE. Finally, we showcased the application of this system in free-space and underwater hybrid LIDAR for imaging remote objects. We believe that this work has further

advanced the research field of polarization-insensitive SNSPDs and has expanded their application spaces.

Disclosures. The authors declare no conflicts of interest.

Data availability. Data underlying the results presented in this paper are not publicly available at this time but may be obtained from the authors upon reasonable request.

Supplemental document. See Supplement 1 for supporting content.

REFERENCES

1. Y. Meng, K. Zou, N. Hu, L. Xu, X. Lan, S. Steinhauer, S. Gyger, V. Zwiller, and X. Hu, ACS Photonics **9**, 1547 (2022).
2. K. Wei, W. Zhang, Y.-L. Tang, L. You, and F. Xu, Phys. Rev. A **100**, 022325 (2019).
3. N. Hu, Y. Meng, K. Zou, Y. Feng, Z. Hao, S. Steinhauer, S. Gyger, V. Zwiller, and X. Hu, Optica **9**, 346 (2022).
4. Y. Xiao, S. Wei, J. Xu, R. Ma, X. Liu, X. Zhang, T. H. Tao, H. Li, Z. Wang, L. You, and Z. Wang, ACS Photonics **9**, 3450 (2022).
5. H. Li, H. Wang, L. You, P. Hu, W. Shen, W. Zhang, X. Yang, L. Zhang, H. Zhou, Z. Wang, and X. Xie, Opt. Express **27**, 4727 (2019).
6. H. Wang, P. Hu, Y. Xiao, X. Zhang, H. Zhou, W. Zhang, H. Li, L. You, and Z. Wang, IEEE Photonics J. **14**, 1 (2022).
7. B. S. Robinson, A. J. Kerman, E. A. Dauler, R. J. Barron, D. O. Caplan, M. L. Stevens, J. J. Carney, S. A. Hamilton, J. K. Yang, and K. K. Berggren, Opt. Lett. **31**, 444 (2006).
8. F. I. Khatri, B. S. Robinson, M. D. Semprucci, and D. M. Boroson, Acta Astronaut. **111**, 77 (2015).
9. A. McCarthy, N. J. Krichel, N. R. Gemmell, X. Ren, M. G. Tanner, S. N. Dorenbos, V. Zwiller, R. H. Hadfield, and G. S. Buller, Opt. Express **21**, 8904 (2013).
10. G. Schirripa Spagnolo, L. Cozzella, and F. Leccese, Sensors **20**, 2261 (2020).
11. Z.-M. Li, H. Zhou, Z.-Y. Li, Z.-Q. Yan, C.-Q. Hu, J. Gao, S.-B. Wu, S.-Y. Yin, and X.-M. Jin, Opt. Express **29**, 28124 (2021).
12. S. Chen, L. You, W. Zhang, X. Yang, H. Li, L. Zhang, Z. Wang, and X. Xie, Opt. Express **23**, 10786 (2015).
13. D. J. Segelstein, "The complex refractive index of water," Ph.D. thesis, University of Missouri–Kansas City (1981).